Microwave Metasurface Cloaking for Freestanding Objects

Hakjune Lee● and Do-Hoon Kwon●*

*Department of Electrical and Computer Engineering, University of Massachusetts Amherst,
Amherst, Massachusetts 01003, USA*

Since the introduction of transformation optics and experimental demonstration using microwave metamaterials in 2006, a variety of electromagnetic invisibility cloaking techniques and physical realizations based on coordinate transformations, scattering cancellation, and control of reflected and transmitted waves have been reported from microwaves to visible. However, existing cloaking methodologies face challenges in reducing cloak thicknesses, concealing large volumes, and cloaking free-standing objects. Here, we design, fabricate, and experimentally validate a unidirectional, single-layer printed metasurface cloak for free-standing cylindrical objects in the microwave regime. Based on a spatially modulated reactance surface, the printed metasurface converts an incident plane wave on the lit side into a surface wave, which carries power to the shadow side before reconstructing the incident wave behind the object. Using a subwavelength-thin printed circuit prototype, the cloaking function is experimentally confirmed, demonstrating a thin, passive cloak that conceals a large, free-standing object.

I. INTRODUCTION

Achieving perfect electromagnetic cloaking for large objects is an important step of invisibility research toward practical applications. To date, a few technical approaches have been proposed and experimentally validated for electromagnetic and optical invisibility cloaking. Derived from coordinate mapping [1], transformation optics-based cloaks are volumetric, characterized by inhomogeneous and anisotropic medium parameters—the permittivity ϵ and the permeability μ. Realized using metamaterials [2], a variety of transformation optics cloaks have been proposed and demonstrated for free-standing scatterers [3,4] and for objects placed on a ground plane [5–10]. Metamaterial realizations not only require design and arrangement of complex resonant inclusions, but medium parameter values over a wide range tend to make experimental cloak dimensions as large as or larger than the cloaked region. Such structural complexity and large cloak dimensions limit their practical utility.

Derived from a scattering cancellation approach, plasmonic or mantle cloaking has been proposed and demonstrated [11–14], where the dominant scattering contribution is minimized using a scatterer-dependent thin enclosing shell. While there have been attempts to extend the applicable scatterer dimension [15], the scattering cancellation approach has been proven to be effective in the quasistatic regime. Using multilayered reactance surfaces can extend the dimension of a scatterer beyond the quasistatic limit for effective cloaking [16]. As a thin surface or film variant of volumetric metamaterials, electromagnetic metasurfaces can control wave radiation, propagation, and scattering behaviors using a thin engineered surface [17]. Metasurface cloaks based on the generalized Snell's laws [18] have been demonstrated for hiding objects on a reflecting plane [19,20]. They can hide large objects, and reflective metasurfaces can be realized as a simple structure, typically comprising one layer of resonators over a ground plane. However, they fail for objects that cast a shadow, most notably all free-standing bodies. While applicable to free-standing scatterers, a hybrid cloak utilizing a refracting metasurface still requires a volumetric zero-index material [21]. If wave penetration into the cloaked region is allowed, a waveguide structure can be devised for the incident wave to pass through the region and emerge on the other side for cloaking, as was demonstrated to conceal an array of metallic cylinders inside a waveguide [22]. Active electromagnetic cloaks absorb the illuminating energy on the lit side and emit propagating waves on the shadow side to minimize scattering in all directions [23,24]. Careful coordination of absorption and radiation by active and lossy elements has its own challenges in incident wave sensing and mutual coupling, in addition to potential instabilities associated with amplifiers.

Going beyond tailoring propagating wave fronts, metasurfaces of subwavelength spatial resolutions are capable of controlling evanescent or surface-wave (SW) behaviors.

---

*dhkwon@umass.edu

For overall power-preserved wave-transformation functions, a 100% power-efficient conversion typically results in surfaces having alternatingly active and lossy specifications. Originally proposed to achieve perfect transmissive wave transformations using planar passive metasurfaces [25,26], the evanescent wave control capability can be exploited by purposefully introducing auxiliary SWs to synthesize all-passive surfaces for perfect wave control. For a subwavelength conducting cylinder, a conformal sinusoidally modulated microstrip metasurface alleviated scattering by introducing an SW [27]. Characterized by one or more layers of position-dependent reactive sheet impedances, metasurface designs incorporating auxiliary SW control promise other functionalities [28,29] as well as enhanced performance for existing applications. [30–33]. While the optimization is simple, employing orthogonally polarized SWs results in inhomogeneous and anisotropic surface parameters [28,29], posing a significant realization challenge especially at subwavelength spatial resolutions.

In this paper, a thin microwave metasurface cloak for large, free-standing objects is demonstrated in two dimensions. In the form of a conformal printed conductor strip array on a grounded dielectric substrate, the printed metasurface cloak conceals a circular cylindrical region by reconstructing the incident wave in the shadow region assisted by co-polarized SWs. The length-modulated strips represent a penetrable modulated reactance surface. The modulation profile is determined from synthesis of the complete—propagating and evanescent—field on the top surface of the dielectric substrate associated with the cloaking functionality. Specifically, we design and realize a cylindrical printed metasurface cloak of a four-wavelength diameter in the microwave regime. The cloaking function is experimentally verified by a field-mapping measurement and scattering cross section comparison for a conductor cylinder with and without the cloak.

II. FIELD SYNTHESIS

Illustrated in Fig. 1, we aim to achieve metasurface cloaking using a set of auxiliary SWs to hide a 2D cylindrical object of radius b. Using an $e^{j\omega t}$ time convention, a $+x$-propagating plane wave illuminates the cylinder with the incident E field given by $\mathbf{E}^i = \hat{z}E_z^i = \hat{z}E_0^i e^{-jkx}$ V/m ($k =$ free-space wave number) with an amplitude E_0^i in TE polarization. The metasurface converts the incident wave into SWs and guides them on the lit side along the curved boundary. On the shadow side, propagating waves are continuously leaked in the forward direction. Working in the cylindrical (ρ, ϕ, z) coordinates, the complete fields in $\rho \geq a$ are uniquely determined in terms of the tangential E_z field at $\rho = a = b + t$, where t is the thickness of the dielectric substrate. We introduce and synthesize TE-polarized SWs on the surface at $\rho = a$, $E_{tz}^{SW}(\phi) = E_z^{SW}(\rho = a, \phi)$, in the form
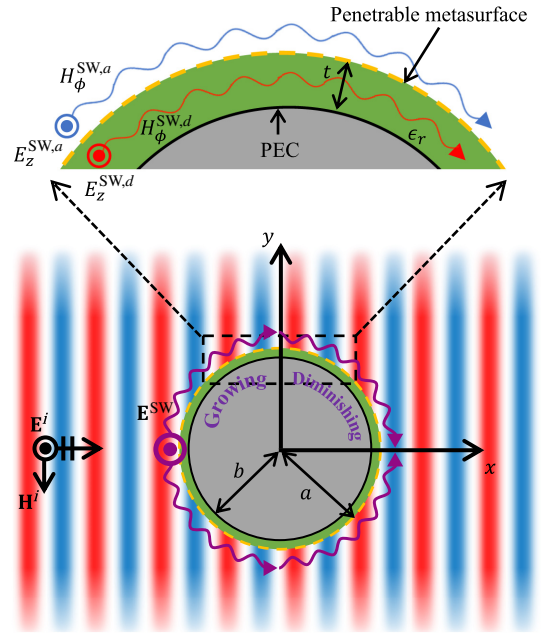

FIG. 1. Configuration of a cylindrical metasurface cloak in 2D TE polarization. The metasurface is given by a penetrable impedance sheet on a grounded dielectric substrate mounted on a cylinder. Subject to a plane-wave illumination, the metasurface induces SWs for eliminating reflections and restoring the incident wave behind the cylinder.

$$E_{tz}^{SW}(\phi) = \underbrace{E_1(\phi)e^{jk_c a|\phi|}}_{E_{1z}^{SW}(\phi)} + \sum_{n=2}^{N} \underbrace{E_n(\phi)e^{j\psi_n(\phi)}}_{E_{nz}^{SW}(\phi)}, \quad -\pi < \phi \leq \pi. \quad (1)$$

This follows a similar functional form as the tangential field synthesis in planar leaky-wave antennas in Ref. [30]. Apart from the curved interface, the main distinction is that Eq. (1) represents a tangential E field on a *penetrable* interface rather than an impenetrable boundary [30]. In Eq. (1), k_c is the carrier propagation constant chosen in the invisible region ($k_c > k$), $\psi_n(\phi) = n\Delta\psi(\phi) + \psi_0(\phi)$, and $\Delta\psi(\phi) = k_c a|\phi| - \psi_0(\phi)$ with $\psi_0(\phi) = \angle E_z^i(\rho = a, \phi)$. The functions $E_1(\phi)$ and $E_n(\phi)$ ($n = 2, \ldots, N$) are real- and complex-valued envelopes for the dominant SW and the higher-order SW terms, respectively. The ϕ-dependent phases of the higher-order SW terms are designed to facilitate destructive interference in the power density for the total fields. Outside (air) and inside (dielectric) the reactance surface at $\rho = a$, the SW E field, $E_z^{SW}(\rho, \phi)$, are separately given by cylindrical harmonic expansions in terms of $E_{tz}^{SW}(\phi)$ as

$$E_z^{SW,a}(\rho, \phi) = \sum_{n=-\infty}^{\infty} a_n \frac{H_n^{(2)}(k\rho)}{H_n^{(2)}(ka)} e^{jn\phi}, \quad \rho \geq a, \quad (2)$$

$$E_z^{\mathrm{SW},d}(\rho,\phi) = \sum_{n=-\infty}^{\infty} a_n \frac{H_n^{(1)}(k_d\rho)H_n^{(2)}(k_db) - H_n^{(1)}(k_db)H_n^{(2)}(k_d\rho)}{H_n^{(1)}(k_da)H_n^{(2)}(k_db) - H_n^{(1)}(k_db)H_n^{(2)}(k_da)} e^{jn\phi}, \; b \le \rho \le a, \tag{3}$$

respectively, where $k_d = k\sqrt{\epsilon_r}$ is the wave number in the dielectric and

$$a_n = \frac{1}{2\pi}\int_{-\pi}^{\pi} E_{tz}^{\mathrm{SW}}(\phi)e^{-jn\phi}d\phi. \tag{4}$$

In Eq. (3), $H_n^{(1)}(\cdot)$ and $H_n^{(2)}(\cdot)$ are the Hankel functions of order n of the first and the second kind, respectively. The ϕ component of the H field outside and inside the reactance surface associated with Eqs. (2)–(3) are found from Maxwell's equations, expressed as

$$H_\phi^{\mathrm{SW},a}(\rho,\phi) = -\frac{j}{\eta}\sum_{n=-\infty}^{\infty} a_n \frac{H_n^{(2)\prime}(k\rho)}{H_n^{(2)}(ka)}e^{jn\phi}, \; \rho \ge a, \tag{5}$$

$$H_\phi^{\mathrm{SW},d}(\rho,\phi) = -\frac{j}{\eta_d}\sum_{n=-\infty}^{\infty} a_n \frac{H_n^{(1)\prime}(k_d\rho)H_n^{(2)}(k_db) - H_n^{(1)}(k_db)H_n^{(2)\prime}(k_d\rho)}{H_n^{(1)}(k_da)H_n^{(2)}(k_db) - H_n^{(1)}(k_db)H_n^{(2)}(k_da)} e^{jn\phi}, b \le \rho \le a, \tag{6}$$

respectively, and a prime indicates differentiation with respect to the whole argument. The intrinsic impedances of free space and the dielectric material are denoted by $\eta \approx 377\ \Omega$ and $\eta_d = \eta/\sqrt{\epsilon_r}$, respectively. Across the penetrable metasurface at $\rho = a$ on a grounded dielectric substrate, the electric field is continuous, but the tangential magnetic field has a discontinuity between $H_{t\phi}^{\mathrm{SW},a}(\phi) = H_\phi^{\mathrm{SW},a}(\rho = a, \phi)$ and $H_{t\phi}^{\mathrm{SW},d}(\phi) = H_\phi^{\mathrm{SW},d}(\rho = a, \phi)$.

In order to obtain a passive and lossless metasurface specification, we optimize the SW E field in Eq. (1) and enforce the local lossless and gainless condition all along the metasurface circumference. Specifically, the envelopes $E_n(\phi)$ $(n = 2, \ldots, N)$ are numerically optimized such that there is no net power generation nor absorption at every ϕ at $\rho = a$. Let us denote the total tangential E-field and the H-field discontinuity as $E_{tz}^{\mathrm{tot}}(\phi) = E_{tz}^i(\phi) + E_{tz}^{\mathrm{SW}}(\phi)$ and $\Delta H_{t\phi} = H_{t\phi}^i(\phi) + H_{t\phi}^{\mathrm{SW},a}(\phi) - H_{t\phi}^{\mathrm{SW},d}(\phi)$, respectively. We require

$$\Delta S_\rho(\phi) = -\frac{1}{2}\,\mathrm{Re}\left\{E_{tz}^{\mathrm{tot}}(\phi)\Delta H_{t\phi}^*(\phi)\right\} \to 0, \forall \phi \in [-\pi, \pi]. \tag{7}$$

While enforcement of Eq. (7) at all $\rho = a$ interface points is impossible, an approximate satisfaction can be obtained by minimizing an error metric, e_{sq}, defined as

$$e_{\mathrm{sq}} = \frac{1}{e_0}\int_{-\pi}^{\pi}|\Delta S_\rho(\phi)|^2 d\phi, \; e_0 = \int_{-\pi}^{\pi}|S_0(\phi)|^2 d\phi, \tag{8}$$

where $S_0(\phi) = -\mathrm{Re}\{E_z^i H_\phi^{i*}\}/2$. The E-field envelopes, $E_n(\phi)$, are defined in terms of their sampled values at preset angular locations. In this work, the *fminsearch* function in MATLAB is used to minimize e_{sq} with respect to the field envelopes.

Once the optimization achieves a low threshold value for e_{sq}, we find the total tangential fields associated with an all-reactive surface specification for metasurface cloaking. The scalar surface impedance $Z_s(\phi)$ is retrieved from the penetrable impedance transition condition as

$$Z_s(\phi) = R_s(\phi) + jX_s(\phi) = \frac{E_{tz}^i(\phi) + E_{tz}^{\mathrm{SW}}(\phi)}{H_{t\phi}^i(\phi) + H_{t\phi}^{\mathrm{SW},a}(\phi) - H_{t\phi}^{\mathrm{SW},d}(\phi)}. \tag{9}$$

The optimization process achieves $R_s(\phi) \approx 0$, so that the impedance surface is characterized by a position-dependent surface reactance $X_s(\phi)$ only.

In this work, the target dimension of our cloak design is selected to be $a = 61.85$ mm $\approx 2\lambda$ ($\lambda =$ free-space wavelength $= 30$ mm) at 10 GHz. A circular cylinder of radius $b = 60.33$ mm is covered by a printed metasurface on a Rogers RO3003 substrate with a relative permittivity $\epsilon_r = 3.0$ and a thickness $t = 1.524$ mm. A penetrable reactance sheet is placed on the cylindrical surface at $a = b + t = 61.85$ mm. Internal to the cloak an aluminum cylinder is placed, modeled as a perfect electric conductor. In the field synthesis for the target cylinder, we choose $k_c = 2k$ in the invisible region and employ SWs up to the seventh-order term (i.e., $N = 7$), which leads to the optimization reaching $e_{\mathrm{sq}} = 5 \times 10^{-4}$. The synthesized $Z_s(\phi)$ is shown in Fig. 2(c).
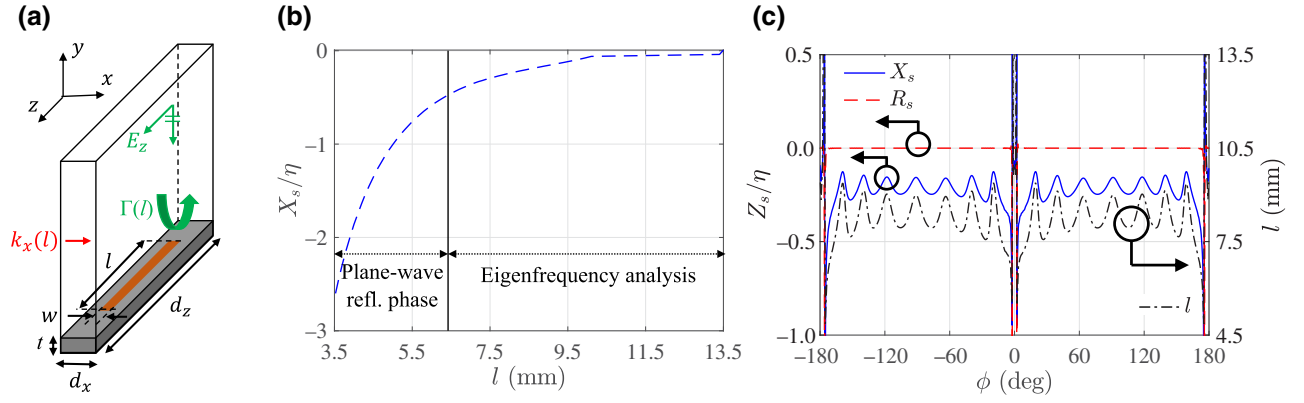
FIG. 2. Unit-cell configuration and analysis for physical printed metasurface design. (a) The unit cell comprising a printed copper strip on a grounded dielectric substrate. (b) The design curve for the surface reactance with respect to the strip length l at 10 GHz. (c) The metasurface specification as a surface reactance distribution together with the associated copper strip lengths.

III. PRINTED METASURFACE DESIGN

In order to physically realize the synthesized surface reactance distribution, we employ an array of z-directed conductor strips on a grounded dielectric substrate, wrapped around into a cylindrical shell. Each strip is designed assuming a planar doubly periodic array environment, which is capable of supporting TE SWs exploited in the cloak design. Figure 2(a) illustrates the unit cell of dimensions $d_x \times d_z$ in the x-z plane having a thin copper strip of length l and width w on a grounded dielectric substrate of thickness t. Using the transverse resonance condition for the equivalent transmission-line circuit [34], the surface impedance can be retrieved as

$$Z_s(l) = \frac{-jk\eta}{jk_y^a(l) + k_y^d(l)\cot[k_y^d(l)t]},\qquad(10)$$

where

$$k_y^a(l) = \begin{cases} \sqrt{k^2 - k_x(l)^2}, & k \geq k_x(l) \\ -j\sqrt{k_x(l)^2 - k^2}, & k < k_x(l) \end{cases},\qquad(11)$$

$$k_y^d(l) = \begin{cases} \sqrt{k_d^2 - k_x(l)^2}, & k_d \geq k_x(l) \\ -j\sqrt{k_x(l)^2 - k_d^2}, & k_d < k_x(l) \end{cases}.\qquad(12)$$

In Eqs. (11)–(12), $k_x(l)$ is the propagation constant along the x axis of the eigensolution to the periodic unit cell under the phase-shift boundary conditions. The eigenfrequency solutions in this study are obtained using COMSOL Multiphysics.

The transverse resonance condition reveals that a TE-polarized SW is supported with a capacitive reactance in $X_s/\eta > -0.3427$. For the printed conductor strip array under consideration, this reactance range corresponds to $l > 6.4$ mm. In the case of a short $l < 6.4$ mm, bound SW eigenmodes do not exist, so we retrieve the surface

impedance via plane-wave reflection phase simulations. The simulation finds a reflection coefficient $\Gamma(l)$ when an x-polarized plane wave illuminates the unit cell at normal incidence. Then, the surface impedance is evaluated as

$$Z_s(l) = j\left[\frac{1}{\eta}\tan\frac{\angle\Gamma(l)}{2} - \frac{1}{\eta_d}\cot(k_d t)\right]^{-1}.\qquad(13)$$

Since only lossless materials are assumed in the simulation, the surface impedance is purely imaginary, as can be seen in Eqs. (10) and (13).

For the geometrical parameters in this work given by $d_x = 0.71$, $w = d_x/2 = 0.35$, $d_z = 0.45\lambda = 13.5$, $t = 1.524$ (all in millimeters), and the relative permittivity $\epsilon_r = 3.0$ of the Rogers RO3003 laminates, the design curve is completed by combining the results from the two methods, as shown in Fig. 2(b). Applying the design curve to the synthesized surface reactance distribution $X_s(\phi)$ of the cloak, the lengths of all 574 copper strips are determined, as shown in Fig. 2(c).

IV. SIMULATION RESULTS

To predict the cloaking performance of the fabricated metasurface, scattering characteristics are simulated using COMSOL Multiphysics incorporating all structural and material details. A snapshot of the simulated total E-field distribution is plotted in Fig. 3(a) when the cloak is subject to a unit plane-wave illumination with $\mathbf{E}^i = \hat{z}e^{-jkx}$ V/m. The E-field distributions clearly show that the incident wave is reconstructed in the shadow region and a small amount of backward scattering is observed. We can see that the intended SWs tightly bound to the metasurface are induced for carrying power from the lit side to the shadow side. Magnified views in Figs. 3(b) and 3(c) show fields near the strip array surface, in both internal and external regions. This validates the surface reactance synthesis
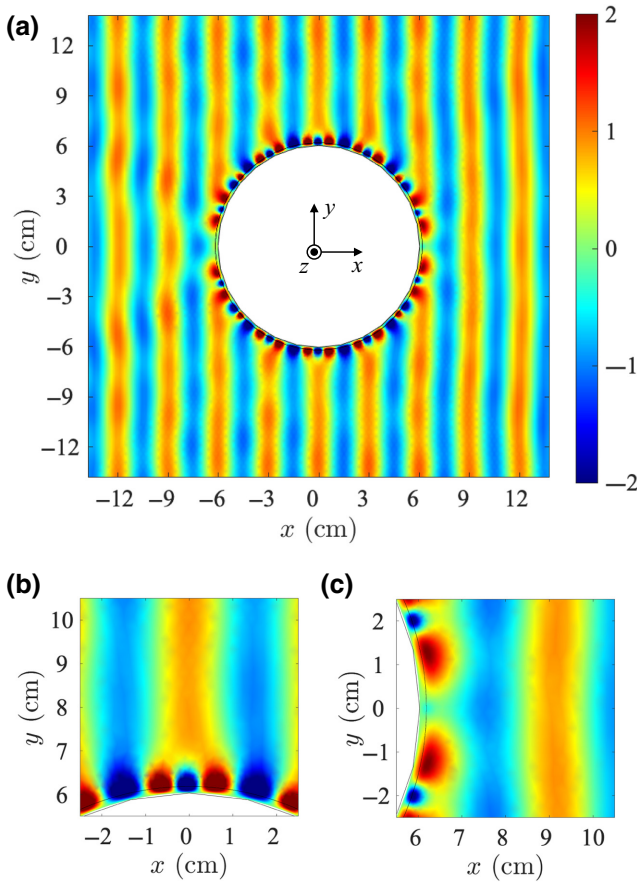
FIG. 3.   Full-wave simulation results for the printed metasurface design at 10 GHz. (a) A snapshot of the total E-field distribution in V/m for the cylindrical cloak. (b)–(c) Magnified views near the topmost and rightmost parts of the cloak.

approach using a penetrable impedance sheet that correctly incorporates the grounded dielectric configuration.

V. MEASUREMENT SETUP

The parallel-plate waveguide simulator [35] used in this work for automated E-field mapping measurement is pictured in Fig. 4(a) with the upper plate lifted open. The field mapper is similar in design and operating principles to the measurement apparatus reported in Ref. [36]. The electromagnetic fields are confined between two parallel aluminum plates with a plate separation of $d_z = 13.5$ mm $< \lambda/2 = 15$ mm, so that only the fundamental transverse electromagnetic (TEM) mode can propagate without attenuation. As the TEM mode has z-invariant fields, we measure $E_z(x, y)$ using a cut-coax E-field sensor embedded at the center of the 1.2×1.2 m^2 upper plate. The scatterer is placed at the center of the 0.9×0.9 m^2 lower aluminum plate attached to computer-controlled XY-translation stages (OptoSigma SGSP46-400). Along one edge of the lower plate, a 32-element linear monopole

array is mounted to generate the incident plane wave in the measurement area, as shown in Fig. 4(b).

For feeding the array antenna, a 1-to-32 unequal power splitter is designed in three cascaded stages [Fig. 4(a)] to minimize ripples in the incident wave in the quiet zone. Design and simulation of the power splitter are performed using CST Studio Suite by Dassault Systèmes. Detailed in Fig. 4(d), the linear array has a uniform spacing of 22.5 mm and it is backed by a vertical conductor wall 7.5 mm behind the array. Lined along the other three edges, the sawtooth-profile foam absorber reduces reflections back into the scanning area. To scan the field automatically, an in-house LABVIEW program handles the motion of the stages with a resolution of 2 mm. The overall scanning area measures 276×276 mm^2. With the upper plate closed [Fig. 4(c)], the complex S_{21} parameter is measured by a vector network analyzer (Model E8363B by Agilent Technologies) between the monopole array port and the E-field sensor port, and recorded on the computer. At each probe position, frequency is swept from 9.5 to 10.5 GHz at an interval of 5 MHz.

VI. MEASUREMENT RESULTS

A metasurface prototype is fabricated using standard printed-circuit technologies at an external fabrication house. Figure 5(a) shows a photo of the fabricated cloak mounted on an aluminum disc of radius b with a detailed view of the length-modulated copper strips. As shown in Fig. 5(b), each cell contains one copper strip of length l. Fixed dimensions of the unit cell and the conductor strip are also shown. The cell height is equal to d_z in the z direction and the cell width $w \approx \lambda/42.3$ so that 574 cells comprise the metasurface. A thin layer of steel wool is placed on top of the aluminum disc to electrically seal the unavoidable narrow gap between the top waveguide plate and the aluminum disc in the parallel-plate waveguide measurement setup.

The cloaking performance is evaluated by measuring the electric field distribution in the x-y plane near the cloak. Three cases are measured for E-field distributions: an empty 2D space (free space) for the incident wave, with a bare aluminum cylinder with radius $b = 60.33$ mm as a reference scatterer, and with the thin metasurface cloak applied onto the cylinder surface as a cylindrical sleeve. The measured field snapshots at 10.0 GHz are shown in Fig. 6. The measured incident field in Fig. 6(a) shows linear wave fronts associated with $+x$-axis propagation with minor magnitude variations. When the bare aluminum cylinder is placed, strong interference patterns (standing waves) appear on the left side of the scatter and a deep shadow is cast on the right side, as expected. Once the thin metamaterial cloak is applied to the aluminum cylinder surface, strong SWs are detected on and near the cloak surface, as is designed and confirmed by
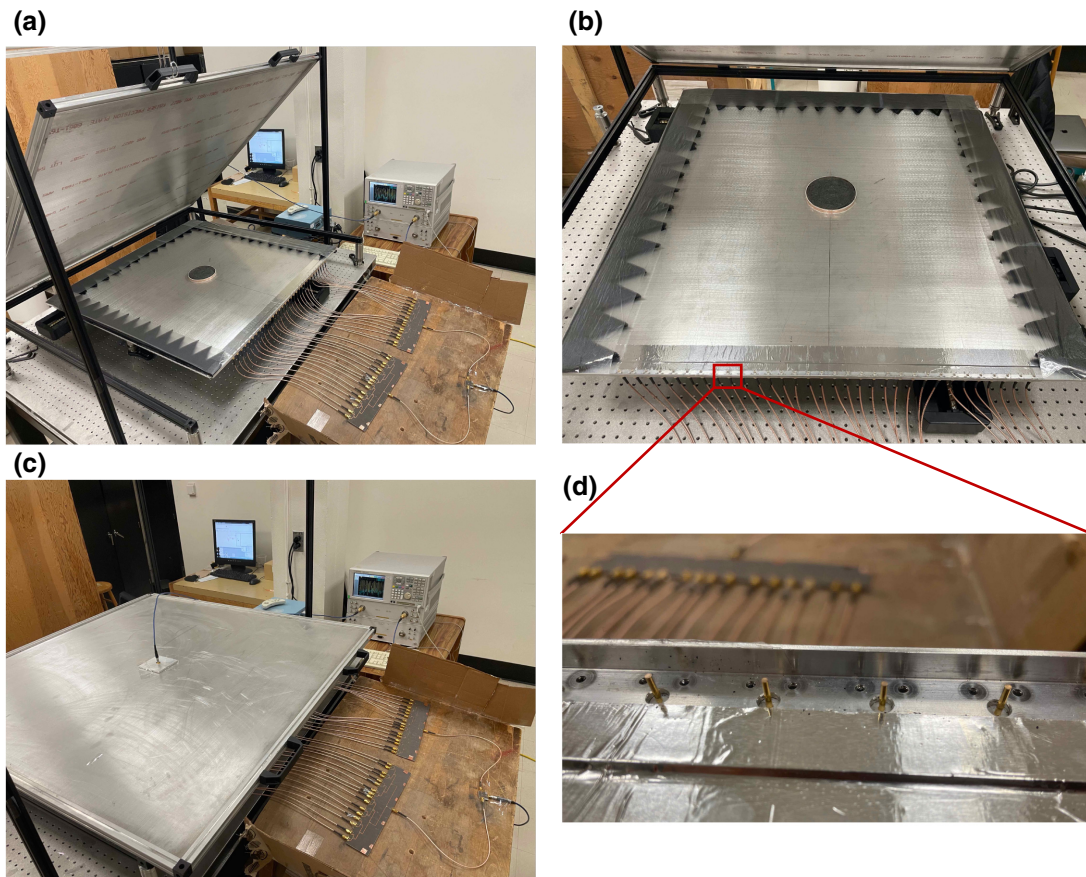
FIG. 4. Photographs of the 2D field mapper and measurement setup. (a) The overall configuration with the upper plate of the parallel-plate waveguide open. (b) The scattering object, absorber, and monopole array placed on the lower plate. (c) The closed waveguide simulator and the electric field probe mounted at the center of the upper plate. (d) A magnified view of the monopole array elements.

simulation. Remarkably, the incident wave is restored in the shadow region, and the intensity of the reflected wave in the backward direction is significantly reduced.
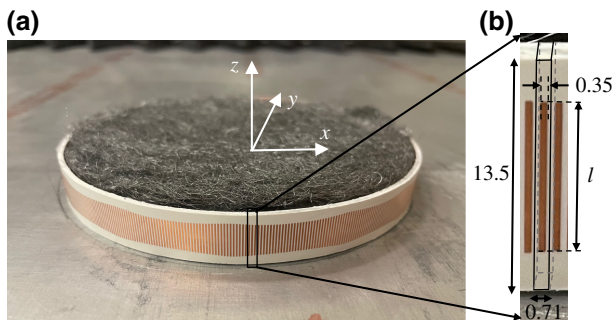

FIG. 5. Printed metasurface cloak as a length-modulated copper strip array on a band of grounded dielectric substrate. (a) Photograph of the fabricated cloak enclosing a cylindrical object in the parallel-plate waveguide field mapper with the top plate open. Steel wool is used to prevent a wave from propagating between the upper plate and the cloak. (b) A detailed view of individual cells. All fixed dimensions are in millimeters.

Minor imperfections are observed in the measured fields in Fig. 6. Backward reflection is still present. The phase of the reconstructed wave behind the cylinder exhibits a small deviation from that of the incident wave. Fabrication error and measurement imperfections cause degradation of the cloaking performance. The permittivity of the dielectric substrate may be slightly different from the nominal value. The resulting modification of the SW phase velocity leads to a phase error for the reconstructed wave behind the cylinder. While low-loss constituents are used, dielectric and conductor losses inevitably weaken the reconstructed wave strength. The cloak is designed for plane-wave illumination, but the array-generated incident wave deviates from a plane wave. Despite these minor imperfections, the printed metasurface clearly demonstrates cloaking for the cylinder of a 4λ diameter.

To assess the quantitative performance of the cloak with respect to frequency, we evaluate the 2D bistatic radar cross section (RCS) or scattering width $\sigma_{2D}(\phi)$ [37]. Since measurement data only for the E field in the near-field region are available, the bistatic RCS is retrieved using
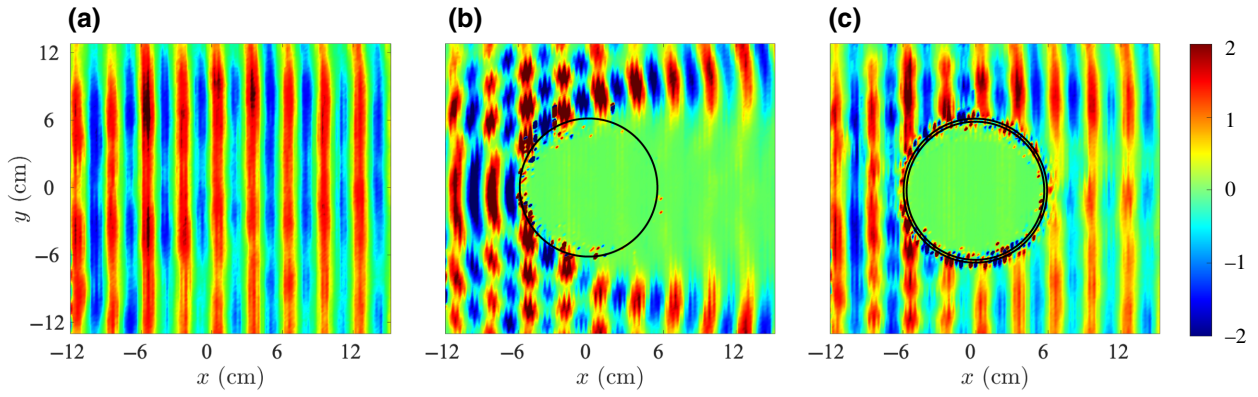
FIG. 6.   Instantaneous snapshots of the measured electric field distribution normalized by the rms average magnitude of the measured incident electric field at 10.0 GHz. (a) The incident wave. (b) For a bare aluminum cylinder. (c) For the aluminum cylinder covered by the metasurface cloak. Thin black circles indicate the boundaries of the conductor cylinder and the cloak. The three plots share the color scale shown at the far right in arbitrary units.

the surface equivalence theorem [38]. The detailed process is as follows: (1) The measured total E_z is sampled along an imaginary circle surrounding the aluminum disc and the cloak. (2) The incident E field, E_z^i, is sampled along the same circle from a separate measurement without any scatterer. (3) The scattered E field ($E_z^s = E_z - E_z^i$) is computed as the difference between the measured electric fields with and without the scatterer. (4) An impressed magnetic surface current $\mathbf{M}_s(\phi') = \hat{\phi}' E_z^s(\phi')$ is placed along the imaginary circle with its entire internal region filled with a perfect electric conductor. (5) The bistatic 2D scattering width is obtained from the far-zone radiated E-field pattern generated by $\mathbf{M}_s$. COMSOL Multiphysics is used to perform this near field–far field transformation. The scattering results for the bare aluminum disc serve as a reference for quantifying the cloaking effectiveness.

At 10.0 GHz, Fig. 7(a) compares the 2D bistatic RCS patterns of the bare and cloaked cylinders. It can be seen that the bistatic RCS is significantly reduced in almost all directions by the metasurface cloak. The RCS is reduced by 7.95 dB in the forward direction ($\phi = 0$), which is the direction of strongest scattering. In other directions, the metasurface weakens scattering to low levels, including a backscattering RCS of less than 5 dBλ. Bistatic 2D scattering widths normalized by λ at 10.0 GHz in the forward direction are compared in Fig. 7(b) with respect to frequency. The bare aluminum disc scatters strongly for canceling the incident wave and creating a shadow, resulting in a consistently high scattering width value over frequency. In contrast, the metasurface cloak significantly reduces forward scattering by reconstructing the incident wave near 10 GHz. The minimum value is 12.09 dBλ at 10.01 GHz, reduced by 8.22 dB from the bare cylinder case.

To evaluate the overall cloaking performance, we compute an angle-integrated scattering metric for the uncloaked and cloaked objects. The 2D total scattering cross section, σ_{2D}^{tot}, is defined as the 2D counterpart of the total scattering cross section [39,40] as

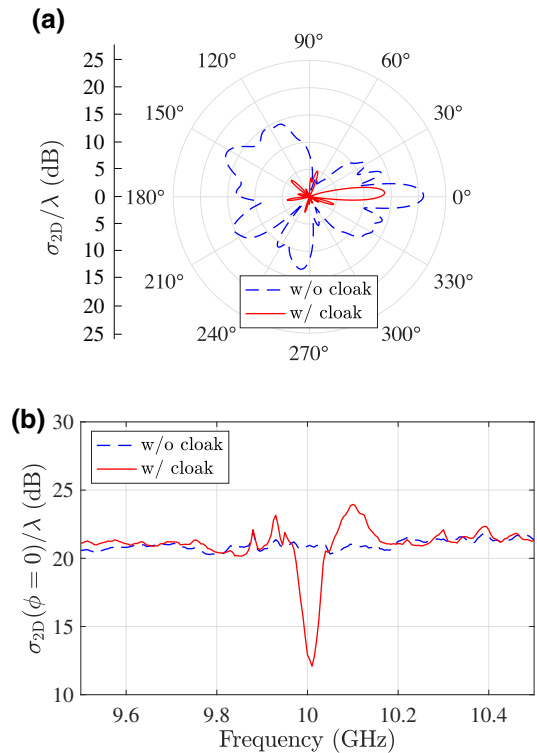$$\sigma_{2D}^{tot} = \frac{1}{2\pi} \int_{-\pi}^{\pi} \sigma_{2D}(\phi) d\phi. \tag{14}$$

FIG. 7.   Measured 2D scattering widths for bare and cloaked discs. (a) The 2D bistatic RCS polar patterns at 10.0 GHz and (b) the RCS in the forward direction ($\phi = 0$) with respect to frequency.
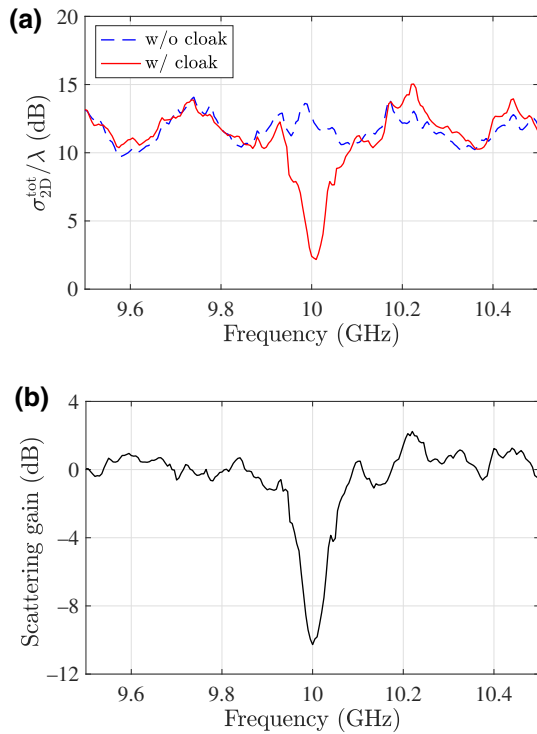
(a)

(b)

FIG. 8. Measured total scattering cross sections. (a) Measured 2D total scattering cross section with and without the cloak. (b) The 2D total scattering cross section gain.

Figure 8(a) plots σ_{2D}^{tot} of the cylinder with respect to frequency with and without the metasurface cloak. For the bare conducting cylinder, the total scattering width stays consistently around 12 dBλ. On the other hand, the cloaked cylinder exhibits significantly reduced scattering around 10 GHz, as expected. The scattering gain is defined as $\sigma_{2D}^{tot}\big|_{cloaked} - \sigma_{2D}^{tot}\big|_{uncloaked}$ in dB scale and plotted in Fig. 8(b). The minimum scattering gain (i.e., maximum scattering reduction) is -10.27 dB at 10.0 GHz. The 3-dB scattering reduction bandwidth is approximately 1.0%, corresponding to 9.95–10.05 GHz. As the frequency deviates from the design frequency, the phase error between the continuously leaked wave and incident wave increases along the metasurface, resulting in an inherently narrow cloaking bandwidth.

Loss effects of the dielectric substrate and copper cladding are numerically evaluated and plotted in Fig. 9. The conductor loss is modeled using an impedance surface with a surface impedance $Z_s = \sqrt{\omega\mu_0/2\sigma_c} = 0.0261\ \Omega/\square$ (μ_0 = free-space permeability) at 10 GHz with the copper conductivity $\sigma_c = 5.8 \times 10^7$ S/m. We find that conductor loss is negligible. As the dielectric loss tangent increases, the SWs will attenuate at a higher spatial rate along the metasurface. As a result, stronger forward scattering occurs, resulting in weaker reconstructed field in the shadow region. At the nominal dielectric loss of the
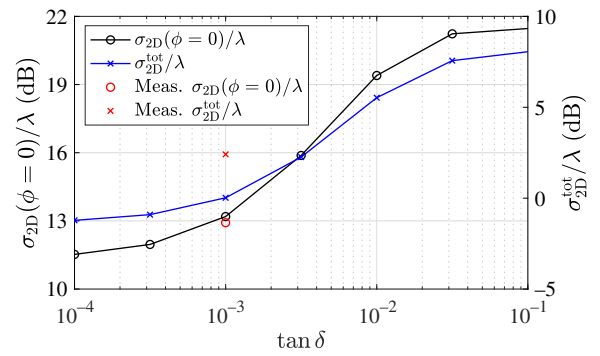

FIG. 9. Simulated and measured 2D scattering width and total scattering section with respect to the dielectric loss tangent of the substrate. Conductor loss of copper is treated using a surface impedance.

substrate ($\tan\delta = 0.001$), measured scattering characteristics show a good agreement with numerical predictions.

VII. CONCLUSION

In the microwave regime, a subwavelength-thin printed metasurface cloak that can conceal a large free-standing object is demonstrated. This capability is enabled by the synthesis of the total tangential field in the entire design domain, assisted by carefully designed auxiliary surface waves. Modeling the reactance surface as a penetrable impedance sheet on a grounded dielectric substrate allows the resulting surface reactance distribution to be accurately realized as an array of length-modulated printed conductor strips. The field synthesis technique for functional reactance surfaces will enable a variety of passive devices for perfect wave transformation in leaky-wave antennas, lenses, and holograms of curved as well as planar profiles.

ACKNOWLEDGMENTS

[1] J. B. Pendry, D. Schurig, and D. R. Smith, Controlling electromagnetic fields, Science **312**, 1780 (2006).

[2] N. Engheta and R. W. Ziolkowski, *Metamaterials: Physics and Engineering Explorations* (Wiley-IEEE press, Hoboken, NJ, 2006).

[3] D. Schurig, J. J. Mock, B. J. Justice, S. A. Cummer, J. B. Pendry, A. F. Starr, and D. R. Smith, Metamaterial electromagnetic cloak at microwave frequencies, Science **314**, 977 (2006).

[4] N. Landy and D. R. Smith, A full-parameter unidirectional metamaterial cloak for microwaves, Nat. Mater. **12**, 25 (2013).

[5] J. Li and J. B. Pendry, Hiding Under the Carpet: A New Strategy for Cloaking, Phys. Rev. Lett. **101**, 203901 (2008).

[6] T. Ergin, N. Strenger, P. Brenner, J. B. Pendry, and M. Wegener, Three-dimensional invisibility cloak at optical wavelengths, Science **328,** 337 (2010).

[7] R. Liu, C. Ji, J. J. Mock, J. Y. Chin, T. J. Cui, and D. R. Smith, Broadband ground-plane cloak, Science **323,** 366 (2009).

[8] C. Qian, B. Zheng, Y. Shen, L. Jing, E. Li, L. Shen, and H. Chen, Deep-learning-enabled self-adaptive microwave cloak without human intervention, Nat. Photon. **14,** 383 (2020).

[9] H. F. Ma and T. J. Cui, Three-dimensional broadband ground-plane cloak made of metamaterials, Nat. Commun. **1,** 21 (2010).

[10] J. Valentine, J. Li, T. Zentgraf, G. Bartal, and X. Zhang, An optical cloak made of dielectrics, Nat. Mater. **8,** 568 (2009).

[11] A. Alù and N. Engheta, Achieving transparency with plasmonic and metamaterial coatings, Phys. Rev. E **72,** 016623 (2005).

[12] A. Alù, Mantle cloak: Invisibility induced by a surface, Phys. Rev. B **80,** 245115 (2009).

[13] D. Rainwater, A. Kerkhoff, K. Merlin, J. C. Soric, G. Moreno, and A. Alù, Experimental verification of three-dimensional plasmonic cloaking in free-space, New J. Phys. **14,** 013054 (2012).

[14] H. M. Bernety and A. B. Yakovlev, Reduction of mutual coupling between neighboring strip dipole antennas using confocal elliptical metasurface cloaks, IEEE Trans. Antennas Propag. **63,** 1554 (2015).

[15] Z. H. Jiang and D. H. Werner, Exploiting metasurface anisotropy for achieving near-perfect low-profile cloaks beyond the quasi-static limit, J. Phys. D: Appl. Phys. **46,** 505306 (2013).

[16] A. Monti, L. Tenuti, G. Oliveri, A. Alù, A. Massa, A. Toscano, and F. Bilotti, in *Proc. 8th Int. Congr. Adv. Electromagn. Mater. Microw. Opt. (Metamaterials 2014)* (Copenhagen, Denmark, 2014), p. 214.

[17] S. B. Glybovski, S. A. Tretyakov, P. A. Belov, Y. S. Kivshar, and C. R. Simovski, Metasurfaces: From microwaves to visible, Phys. Rep. **634,** 1 (2016).

[18] N. Yu, P. Genevet, M. A. Kats, F. Aieta, J.-P. Tetienne, F. Capasso, and Z. Gaburro, Light propagation with phase discontinuities: Generalized laws of reflection and refraction, Science **334,** 333 (2011).

[19] X. Ni, J. Wong, M. Mrejen, Y. Wang, and X. Zhang, An ultrathin invisibility skin cloak for visible light, Science **349,** 1310 (2015).

[20] Y. Yang, L. Jing, B. Zheng, R. Hao, W. Yin, E. Li, C. M. Soukoulis, and H. Chen, Full-polarization 3D metasurface cloak with preserved amplitude and phase, Adv. Mater. **28,** 6866 (2016).

[21] H. Chu, Q. Li, B. Liu, J. Luo, S. Sun, Z. H. Hang, L. Zhou, and Y. Lai, A hybrid invisiblity cloak based on integration of transparent metasurfaces and zero-index materials, Light Sci. Appl. **7,** 50 (2018).

[22] P. Alitalo, F. Bongard, J.-F. Zürcher, J. Mosig, and S. Tretyakov, Experimental verification of broadband cloaking using a volumetric cloak composed of periodically stacked cylindrical transmission-line networks, Appl. Phys. Lett. **94,** 014013 (2009).

[23] M. Selvanayagam and G. V. Eleftheriades, Experimental Demonstration of Active Electromagnetic Cloaking, Phys. Rev. X **3,** 041011 (2013).

[24] D. L. Sounas, R. Fleury, and A. Alù, Unidirectional Cloaking Based on Metasurfaces with Balanced Loss and Gain, Phys. Rev. Appl. **4,** 014005 (2015).

[25] A. Epstein and G. V. Eleftheriades, Synthesis of Passive Lossless Metasurfaces Using Auxiliary Fields for Reflectionless Beam Splitting and Perfect Reflection, Phys. Rev. Lett. **117,** 256103 (2016).

[26] A. Epstein and G. V. Eleftheriades, Arbitrary power-conserving field transformations with passive lossless omega-type bianisotropic metasurfaces, IEEE Trans. Antennas Propag. **64,** 3880 (2016).

[27] L. Matekovits and G. Labate, in *Proc. 46th Eur. Microw. Conf. (EuMC 2016)* (London, UK, 2016), p. 787.

[28] D.-H. Kwon, Lossless tensor surface electromagnetic cloaking for large objects in free space, Phys. Rev. B **98,** 125137 (2018).

[29] D.-H. Kwon, Illusion electromagnetics for free-standing objects using passive lossless metasurfaces, Phys. Rev. B **101,** 235135 (2020).

[30] D.-H. Kwon, Modulated reactance surfaces for leaky-wave radiation based on complete aperture field synthesis, IEEE Trans. Antennas Propag. **68,** 5463 (2020).

[31] J. Budhu and A. Grbic, Perfectly reflecting metasurface reflectarrays: Mutual coupling modeling between unique elements through homogenization, IEEE Trans. Antennas Propag. **69,** 122 (2021).

[32] H. Lee and D.-H. Kwon, Large and efficient unidirectional plane-wave–surface-wave metasurface couplers based on modulated reactance surfaces, Phys. Rev. B **103,** 165142 (2021).

[33] V. G. Ataloglou and G. V. Eleftheriades, Arbitrary wave transformations with Huygens' metasurfaces through surface-wave optimization, IEEE Antennas Wireless Propag. Lett. **20,** 1750 (2021).

[34] O. Luukkonen, C. Simoski, G. Granet, G. Goussetis, D. Lioubtchenko, A. V. Räisänen, and S. A. Tretyakov, Simple and accurate analytical model of planar grids and high-impedance surfaces comprising metal strips or patches, IEEE Trans. Antennas Propag. **56,** 1624 (2008).

[35] C. D. Emiroglu and D.-H. Kwon, Design and realization of virtual line source using metamaterials, IEEE Trans. Antennas Propag. **64,** 5220 (2016).

[36] B. J. Justice, J. J. Mock, L. Guo, A. Degiron, D. Schurig, and D. R. Smith, Spatial mapping of the internal and external electromagnetic fields of negative index metamaterials, Opt. Express **14,** 8694 (2006).

[37] C. A. Balanis, *Advanced Engineering Electromagnetics* (Wiley, New York, 1989).

[38] R. F. Harrington, *Time-Harmonic Electromagnetic Fields* (Wiley-IEEE press, Hoboken, NJ, 2001).

[39] J. D. Jackson, *Classical Electrodynamics* (Wiley, New York, 1999), 3rd ed.

[40] A. V. Osipov and S. A. Tretyakov, *Modern Electromagnetic Scattering Theory with Applications* (Wiley, New York, 2017).